

# Analysis of the Behavior of the Electromagnetic Frequency Regulator (EFR) Used in Hybrid Wind-Solar Photovoltaic Generation Systems.

A. E. S. Costa, A. O. Bissiriou, G. P. de Oliveira, J. V. S. Silva, R. F. Pinheiro and A. O. Salazar

Department of Computer Engineering and Automation  
D.C.A, Federal University of Rio Grande do Norte  
Campus of Lagoa Nova – Natal/RN, 59078-970 (Brazil)  
Phone/Fax number: +55 (84) 3215 3883/1524,

## Abstract.

Within the context of integrating renewable energy sources, the Electromagnetic Frequency Regulator (EFR) presents a promising technology, particularly in hybrid distributed generation systems. This paper conducts a comprehensive analysis of pole pair configurations for both the EFR and the induction generator within such systems to enhance overall performance. An algorithm developed in Scilab is utilized for steady-state analyses considering various configurations. The methodology involves repetitive computations to evaluate the angular velocity of both the EFR and the generator, as well as the transformation ratios of the speed multiplier for different pole pairs. Scenarios with varying combinations of pole numbers are explored, demonstrating the impact on EFR velocity and the drive frequency of the EFR. Results showcase the efficacy of the proposed algorithm, providing insights into the selection of the most appropriate pole pairs to improve system performance.

**Key words.** Renewable Energy, Electromagnetic Frequency Regulator, Induction Generator, Pole Pair Configurations.

## 1. Introduction

Compared to conventional modes of electricity generation, non-dispatchable energy sources, such as solar and wind power, are known for their high degree of uncertainty and unpredictability [1]. Wind power, for example, presents challenges due to its intermittent nature, resulting in fluctuations in turbine output that complicate synchronization with the main grid [2]. Similarly, environmental factors such as irradiance and temperature significantly influence solar power generation performance, further complicating alignment with demand requirements [3]. Additionally, the primary source may present abrupt variations that can be transmitted to the main grid. One potential strategy for mitigating these limitations is to adopt a hybrid Distributed Generation (DG) system that combines Renewable Energy Sources (RESs) such as solar and wind generation [4].

A hybrid system utilizes multiple energy sources to optimize the generation and distribution of electrical energy while minimizing costs and adapting to the variable availability of energy resources [5]. These systems typically integrate RESs, such as solar and wind generation, along with energy storage systems (ESSs),

loads, control devices, and power converters. This combination enhances efficiency and reliability [6] by connecting DC and AC components to their respective subgrids. The interconnection between these two buses is established through a bidirectional converter, which can function as either an inverter or a rectifier depending on the direction of power flow [7]. However, as stated in reference [6], conventional hybrid systems encounter challenges, such as a substantial initial investment, particularly when key generation equipment is imported. The control system can also become complex, especially in large-scale systems. These challenges highlight the need for innovative approaches and solutions to make these systems more accessible, efficient, and manageable.

Recently, a new methodology has emerged that couples wind turbine rotation speed with the high-speed axis of conventional generators. The objective of this new approach is to convert mechanical power from a variable speed shaft to a fixed speed shaft [8]. This innovative system is known as the Electromagnetic Frequency Regulator (EFR). The EFR technology provides greater flexibility for integrating various energy sources, with wind power as the foundational component [9]. The EFR is an adaptation of a conventional induction motor, where the adaptation involves making the stator casing rotate by mechanically coupling it to the wind turbine shaft or the high-speed shaft of the speed multiplier, if present in the configuration. Therefore, the stator casing of the induction motor in the EFR is referred to as the armature. To maintain the three-phase AC supply to the armature windings, collector rings connected by brushes are introduced, as illustrated in Fig. 1. This inverter can draw power from various sources, such as ESSs, solar power, or other generators [8]. As stated by the authors in [10], this frequency inverter that powers the armature winding injects currents that determine the speed of the rotating field. This, in turn, determines the rotor speed when added with the turbine speed. These unique features make the EFR an excellent example of energy hybridization. The EFR's rotor is connected to an induction generator that can be linked to either the grid or local loads. Fig. 2 depicts a simplified schematic diagram of the EFR.

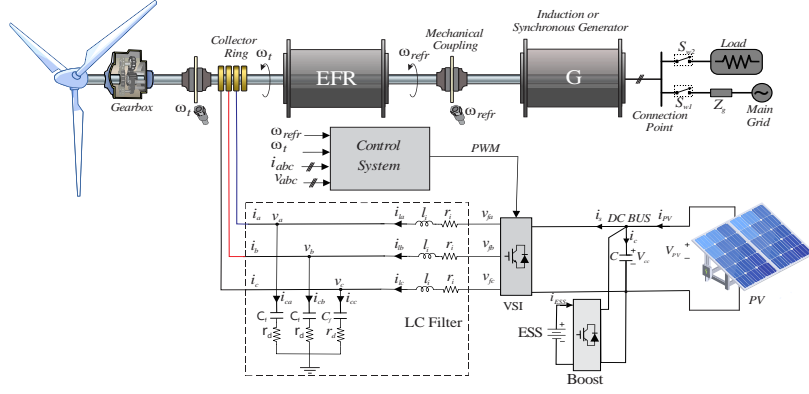


Fig. 1. Hybrid wind-solar photovoltaic generation, including EFR.

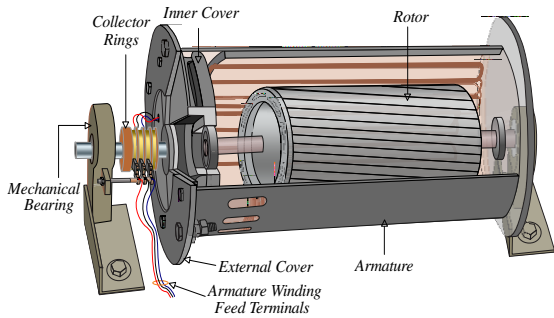


Fig. 2. Cut View of Physical Structure ERF.

Several studies have focused on integrating EFR technology into the interface that connects a wind turbine to a synchronous generator. The initial exploration of EFR was thoroughly described in reference [8], where the authors focused on the mathematical modeling of EFR and its application in regulating frequency generation. Reference [4] proposes using an induction generator connected to the electrical grid, with the EFR controlling the generator shaft speed to achieve maximum power generation at each wind speed. In this paper, the authors maintained the coefficient between the pairs of poles of the EFR and the generator ( $R$ ) constant, equal to one. Alongside this, they kept the transformation ratio of the gearbox unchanged. Through these measures, they were able to operate the system at the Maximum Power Point Tracking (MPPT) by implementing a control strategy on the slip of the EFR. This approach has demonstrated to be a highly effective alternative. Reference [9] presents an extension to the EFR by incorporating a hydrostatic transmission system, replacing the mechanical speed multiplier. In this case, the authors illustrate the operation of the system at the maximum power point. This is accomplished by modifying the transformation ratio ( $N$ ) of the hydrostatic transmission, while maintaining constant the number of poles for both the EFR and the generator ( $PP_g = PP_{efr} = cts$ ). A dynamic modeling and control design for the EFR are presented in [11]. The authors employ the root-locus method (RLM) to determine the parameters of the system controllers, aiming to achieve the desired dynamic performance. Besides, the reference [12] implements a control strategy grounded in Fuzzy theory, employed in the speed control of the EFR in isolated wind generation systems. The aim is to eliminate the control

system's reliance on knowledge of the prototype's physical parameters.

EFR presents several advantages in comparison to alternative systems for integrating renewable sources into the grid: *i*. By generating power through a synchronous generator directly connected to the AC grid, the system can enhance the short-circuit level, thereby increasing the overall inertia of the AC grid; *ii*. Unlike other systems, EFR minimizes dependence on the gearbox, allowing for continuous control over the frequency of the generated voltage. *iii*. The absence of an electronic inverter in the power supply or grid connection preserves power quality. *iv*. The incorporation of a battery bank on the DC side of the inverter ensures a consistent energy supply, overcoming the intermittency of primary sources and enabling dispatchable energy to the main grid. *v*. Lastly, EFR offers the flexibility to hybridize different primary sources.

As detailed in Appendix B of [9], the EFR, characterized by its rotating armature, permits the conceptualization of two types of slip. The first, referred to as the dominated external slip ( $s_{efr0}$ ), is associated with an observer in the stationary reference frame (earth) and aligns with the traditional slip of asynchronous motors (fixed armature). From this perspective, the EFR consistently functions as a motor and exhibits a positive slip, which is nearly zero. The second type, termed as the internal or air gap slip ( $s_{efr}$ ), pertains to an observer situated on the EFR armature, in the region of the air gap. This observer overlooks the rotation of the armature, and perceives the slip as a consequence of the angular velocity imposed by the frequency of the armature currents. As per [9], these two slips are represented by equations (1) and (2), respectively.

$$s_{efr0} = \frac{\omega_{cgefr} - PP_{ref}\omega_{mg}}{\omega_{cgefr}}, \quad (1)$$

and:

$$s_{efr} = \frac{\omega_{tefr} + \omega_{iefr} - PP_{ref}\omega_{mg}}{\omega_{iefr}}, \quad (2)$$

where,  $\omega_{tefr}$  is the armature rotational velocity of EFR,  $\omega_{iefr}$  is the frequency of the currents injected into the armature of EFR,  $\omega_{mg}$  represents the mechanical rotation

speed of the generator, and  $\omega_{cgefr}$  represents the angular frequency the EFR's rotor.

Both the EFR and the induction generator are rotating machines, which can have different numbers of pole pairs. The relationship between the electrical and mechanical speed of the rotor varies depending on the number of EFR pole pairs. This variation affects parameters such as angular velocity, losses, and rotational speed. Therefore, the purpose of this study is to investigate how a change in the pole pair configurations for the EFR and induction generator can impact the maximum power generation of the systems that employ the EFR. An algorithm was developed in Scilab to conduct comprehensive analyses of different pole pair configurations in steady state for both aforementioned elements, taking into account the topology illustrated in Fig. 1.

## 2. Methodology

The methodological considerations adopted in this study involve representing the EFR and the generator as two identical machines that, by adjusting their nominal power, exhibit a slip of 5%. Considered the region of interest, it is defined that the range between  $-5\%$ ,  $0\%$ , and  $+5\%$  of slip in the steady state, losses will be negligible. Taking as reference the equations TxS and PxS of an induction motor [13], whose graphs appear in Fig. 4, it can be observed that within the range of interest ( $-0.05 < s < 0.05$ ), the curves are similar and practically linear.

The electromagnetic torque equation as a function of slip ( $T_e$ ) is obtained by applying Thévenin's theorem to the equivalent circuit of the induction generator between points a and b of Fig. 3(a), looking towards the input terminals of the circuit. The torque value ( $T_{PC}$ ) is then calculated by  $T_{PC} = (T_e/T_N).100$ , where  $T_N$  is the nominal torque.

$$T_e = \frac{1}{\omega_s} \left[ \frac{qV_{1,eq}^2 \frac{R_2}{s}}{\left(R_{1,eq} + \frac{R_2}{s}\right)^2 + (X_{1,eq} + X_2)^2} \right], \quad (3)$$

where  $V_{1,eq}$  is the tension that appears between points a and b of Fig. 3b,  $\omega_s$  is the synchronous speed of the motor in rad/s,  $R_1$  and  $X_1$  are the effective resistance and leakage reactance of the stator, respectively,  $R_2$  and  $X_2$  are the rotor resistance and leakage reactance referenced to the stator, respectively,  $R_{1,eq}$  and  $X_{1,eq}$ , in Fig. 3(b), given by the Thévenin equivalent, are the stator resistance and reactance between terminals a and b of Fig. 3a, and  $s$  represents the motor slip.

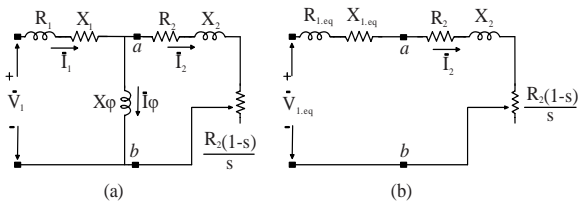


Fig. 3. Equivalent circuits corresponding to (a) the induction motor and its (b) simplified by Thévenin's theorem [13].

Eq. (4) expresses the power as a function of slip, in %, where  $\omega_m = \omega_s(1 - s)$  the angular velocity of the motor.

$$P_{PC} = T_{PC}\omega_m. \quad (4)$$

Considering this aspect, the algorithm presented here was simplified by the use of this linearization, so that these curves are treated, respectively, following equations (5) and (6). The  $P_{PC}$  or  $T_{PC}$  limit at  $+100\%$  corresponds to the action of the EFR at nominal power, while  $P_{PC}$  or  $T_{PC}$  at  $-100\%$  correspond to the action of the induction generator at nominal power.

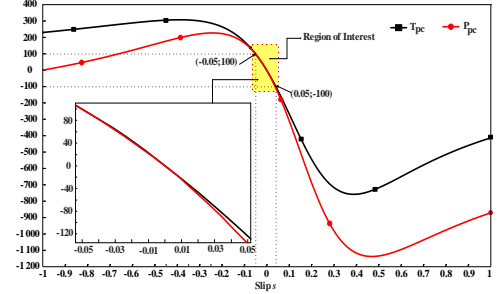


Fig. 4. Combination of T&P versus  $s$ .

An amplified view of the two curves in the region of interest is depicted in detail in Fig. 4.

$$T_{PC} = 2000. s, \quad (5)$$

and

$$P_{PC} = 2000. s, \quad (6),$$

The power versus wind speed (Fig. 5(a)) and turbine shaft speed versus wind speed (Fig. 5(b)) curves were obtained from the results presented in [9]. These results were transported to table I, which allowed establishing a relationship between the turbine's angular speed and the turbined power in percentage values (columns 4 and 3 of table I). This data was then used to create Fig. 6, and an interpolation in Excel was performed to obtain eq. (7). Note that these results from [9] correspond to obtaining the maximum turbine power at each wind speed, as shown in Fig. 5a.

$$\omega_t \approx 39.009. P_t^{0.3339}, \quad (7)$$

where  $\omega_t$  [rpm] is the turbine speed and  $P_t$  the output power of turbine.

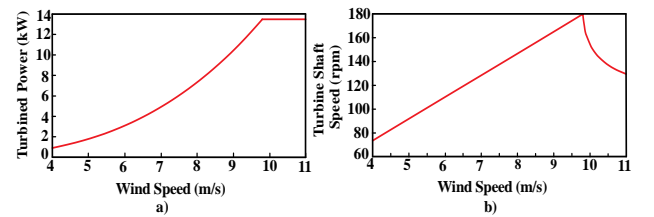


Fig. 5. (a) Behavior of turbine power with wind speed [9]. (b) Relationship between the turbine shaft speed and wind speed [9].

TABLE I.

Turbine Power and Angular Velocity Spreadsheet.

V(m/s)	$P_t$ (kW)	$P_t$ (% $\cdot P_{rate}$ )	$\omega_t$ (rpm)	$\omega_t$ (rad/s)
4	0.9	6.67	74	0.698
5	1.8	13.33	92	1.396
6	3	22.22	110	2.33
7	4.8	35.56	129	3.72
8	7.3	54.074	146	5.66
9	10.5	77.78	165	8.145
10	13.5	100	185	10.47

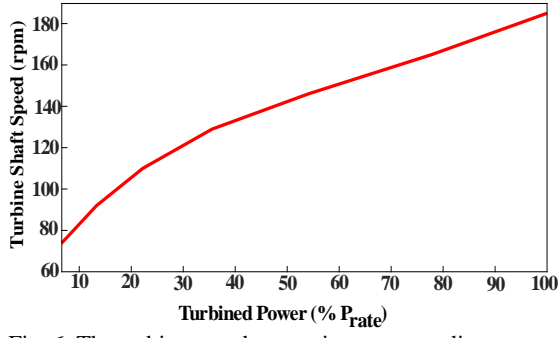


Fig. 6. The turbine speed versus its corresponding power.

To obtain the Fig. 6, the study was carried out by varying the generator power from 0 to 100% at a rate of 10%. The use of percentage power values makes the study generic. Using the algorithm that will be presented in the next section, from the generator power variation, it is possible to calculate the generator speed, the speed of the REF rotor shaft, the EFR torque, the turbine torque, turbine speed and the required wind power.

### 3. Implemented Algorithm

The initial input parameters for the program are summarized in Table II. The algorithm begins by entering the number of poles for both the generator and the EFR, along with the load power. In this study, the turbined power was varied from 10% to 150% in increments of 10%. The EFR rotor shaft speed is calculated by determining the generator speed for each power value. From this, the torque of the EFR is calculated, and the torque on the low-speed side of the turbine is then determined by calculating its speed.

Table II.  
Initial input parameters.

Initial Parameters	Symbology
Pole-pair number of EFR	$PP_{ref}$
Turbine powers	$P_t$
Frequency	$f_g$
Pole-pair number of GER	$PP_g$
Load power in %	$P_l$

1) After introducing the initial parameters into the algorithm, preliminary calculations are performed. Initially, the angular frequency of the generator currents ( $\omega_{ig}$ ) in rad/s is computed using (8), and the mechanical rotation speed of the generator ( $\omega_{mg}$ ) is then given by (9)

$$\omega_{ig} = 2\pi f_g, \quad (8)$$

$$\omega_{mg} = \frac{\omega_{ig}}{PP_g}. \quad (9)$$

The full-load torque on the generator in % is determined using

$$T_l = -\frac{P_l}{\omega_{mg}}. \quad (10)$$

Conceptually, the generator load torque per pole pair ( $T_g$ ) can be defined as follows:

$$T_g = \frac{T_l}{PP_g}. \quad (11)$$

The slip of the generator ( $s_g$ ) in (6) can also be rewritten in term of parameter  $P_l$ , which results in

$$s_g = \frac{-P_l}{2000}. \quad (12)$$

The expression for the synchronous speed of a generator ( $\eta_s$ ) in rpm is given by (13) and the slip effect in an induction machine is simply given by (14)

$$\eta_s = \frac{60f}{PP_g} = \frac{30(\omega_{ig}/\pi)}{PP_g}, \quad (13)$$

$$\eta_g = \eta_s(1 - s_g). \quad (14)$$

From (13) and (14), the rotational speed of the induction generator ( $\eta_g$ ) [rpm] can be calculated as follows:

$$\eta_g = \frac{30(\omega_{ig}/\pi)}{PP_g}(1 - s_g). \quad (15)$$

Conceptually, the EFR's rotational speed  $\eta_{efr}$  is equal to the rotational speed of the generator  $\eta_g$ . Therefore, the angular velocity of EFR  $\omega_{efr}$  [rad/s] is given by

$$\omega_{efr} = \frac{\pi}{30} \cdot \eta_g. \quad (16)$$

Based on (6), the external slip of the EFR  $s_{efr}$  is determined as follows:

$$s_{efr0} = \frac{P_l}{2000}. \quad (17)$$

(17) is the same external slip presented in equation (1). However, in this case, it is an approximation based on the T&P versus s curve, as depicted in Figure 4. The rotating field speed of EFR  $\omega_{cgreff}$  [rad/s] is calculated using the following expression:

$$\omega_{cgreff} = \frac{\omega_{efr} PP_{ref}}{1 - s_{efr0}}. \quad (18)$$

2) Following the initial calculations, repetitive computations are carried out to generate graphical representations illustrating the variations for each pole pair configuration. Hence, the expression for calculating the electromagnetic torque of the EFR  $T_{tefr}$  in % on the high-speed side for each turbine power value  $P_{tk}$ , where k ranges from 1 to n, is as follows:

$$T_{tefr}(k) = -T_l. \quad (19)$$

Based on (19), the angular velocity of EFR in rad/s with reference to the high-speed side is determined by

$$\omega_{tefr}(k) = \frac{P_{tk}}{T_{tefr}(k)}. \quad (20)$$

From (7), the angular velocity of the turbine and EFR armature on the low-speed side in rad/s is given by

$$\omega_{tT}(k) = \frac{\pi}{30} 39 P_{tk}^{0.3339}. \quad (21)$$

Using (21), the velocity of the rotating field of EFR in rpm is determined by the following expression:

$$\eta_{cgreff(k)} = \frac{30 \omega_{tT}(k)}{\pi PP_{efr}}. \quad (22)$$

The transformation ratio between the turbine's angular velocity and the EFR armature on the high-speed side, necessary to achieve the maximum turbine power at wind speed, is determined using (23). Subsequently, the armature rotational velocity, measured in rad/s, is computed using equation (24):

$$N_{rt}(k) = \frac{\omega_{tefr}(k)}{\omega_{tT}(k)}. \quad (23)$$

$$\omega_{tefr}(k) = N_{rt}(k)\omega_{tT}(k). \quad (24)$$

The torque reflected at the turbine side  $T_{tT}$  in % is expressed using (25):

$$T_{tT}(k) = N_{rt}(k)T_{tefr}(k) \quad (25).$$

The contribution of the auxiliary source ( $P_i$ ) in % can be achieved computing the difference between the power supplied to the load and the power extracted from the turbine, which results in the following expression:

$$P_i(k) = P_l - P_t(k) \quad (26).$$

For the EFR, where a mechanical rotation is applied to the armature, the speed of the rotating field is the sum of the angular frequency of the currents at the inverter output ( $\omega_{iefr}$ ) with the mechanical speed of the turbine ( $\omega_{tefr}$ ), expressed as [4]:

$$\omega_{cgefr} = \omega_{iefr} + \omega_{tefr}, \quad (27)$$

here the turbine's mechanical speed needs to be multiplied by  $PP_{ref}$  in the machine to match the angular frequency of the currents at the inverter's output [13]. Thus, using equations (1) and (27),  $s_{efr0}$  can be rewritten as follows

$$s_{efr0} = \frac{\omega_{iefr} + PP_{ref}\omega_{tefr} - PP_{ref}\omega_{mg}}{\omega_{iefr} + PP_{ref}\omega_{tefr}} \quad (28).$$

By isolating  $\omega_{iefr}$  from (28), the frequency of the currents injected into the armature of EFR, in rad/s, is determined as:

$$\omega_{iefr}(k) = \frac{PP_{ref}[\omega_{tefr}(k)(1 - s_{ref}) - \omega_{mg}]}{s_{efr} - 1} \quad (29).$$

From (2) and taking into account the aforementioned factors, the following expression is used to determine the air gap slip of the EFR:

$$s_{efr}(k) = \frac{PP_{ref}\omega_{tefr}(k) + \omega_{iefr}(k) - PP_{ref}\omega_{mg}}{\omega_{iefr}(k)} \quad (30).$$

A simplified flowchart logic algorithm for determining the multiplication ratio for the gearbox, considering the effects of the EFR and generator pole pairs, is shown in Fig. 7.

#### 4. Results

The effectiveness of the proposed algorithm was evaluated using the Scilab software package. The load power was adjusted to 100, and the frequency of the generator currents was set at 60 Hz. The results obtained correspond to 100% of the turbine power. Various combinations were evaluated under diverse scenarios, as presented in Table III.

In this Table III, S1-S6 delineate scenarios in which the number of poles in the EFR remains consistent while the poles of the generator vary. Conversely, G1-G6 denote scenarios where the number of poles in the generator remains constant while those of the EFR system vary.

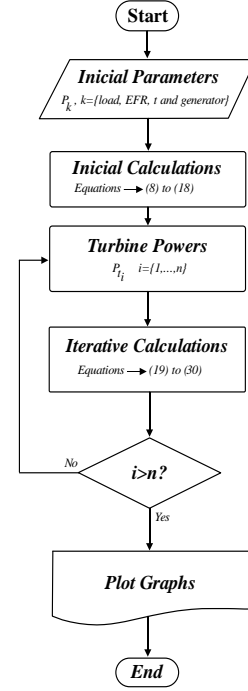


Fig. 7. A simplified flowchart logic algorithm for to analyzing the influence of pole numbers for the EFR and inductance generator.

Table III.  
Scenarios related to different combinations of pole numbers tested.

EFR \ GER	2	4	6	8	10	12	
2	1	1	1	1	1	1	G1
4	1	1	1	1	1	1	G2
6	1	1	1	1	1	1	G3
8	1	1	1	1	1	1	G4
10	1	1	1	1	1	1	G5
12	1	1	1	1	1	1	G6
	S1	S2	S3	S4	S5	S6	

Fig. 8 illustrates the relationship between the angular velocity of the generator and the number of poles in both the generator and the EFR. The graph demonstrates a decrease in the generator's angular velocity as the number of poles in the generator increases, which is consistent with the established properties of induction generators. According to the algorithm presented, the synchronous speed of the generator is inversely related to the number of poles. Therefore, a lower number of poles results in a higher synchronous speed and, consequently, an increased angular velocity of the generator under standard load conditions. Moreover, Fig. 8 also shows that the angular velocity of the generator remains unchanged despite variations in the number of poles in the EFR.

Fig. 9 presents a three-dimensional visualization that demonstrates the impact of the interplay between the

number of pole pairs and the speed multiplication ratio ( $N$ ) on the  $\omega_i$ . This relationship is examined under two distinct scenarios: one with a fixed speed multiplication ratio ( $N$ ), and another where  $N$  is variable. The graph portrays two conditions: when the ratio ( $R$ ) is greater than or equal to 1, it signifies a situation where the number of poles in the generator is equal to or exceeds the number of poles in the EFR. On the other hand, when  $R$  is less than or equal to -1, it indicates a case where the number of poles in the EFR is equal to or surpasses the number of poles in the generator.

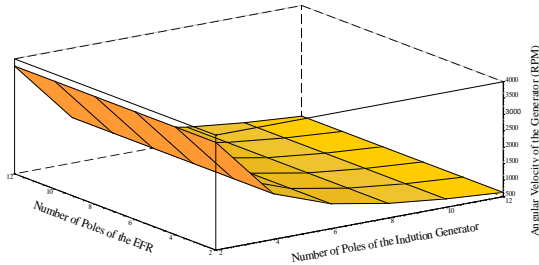


Fig. 8. Angular velocity of the generator in relation to the number of poles of the EFR and the induction generator.

This Fig. 9 delineates two distinct regions. In the first region, where the number of generator poles ( $R$ ) exceeds 1, an increase in the number of generator poles leads to a decrease in both the angular velocity of the EFR currents and the speed multiplication ratio ( $N$ ). This observation is in line with the findings presented in [9], which manipulated the transformation ratio to attain maximum power. In the second region, the number of generator poles is held constant while the number of EFR poles varies ( $R < -1$ ), thereby maintaining  $N$  constant. Under these conditions, the  $\omega_i$  operates within a range of 125.66 rad/s to 753.98 rad/s. These results align with those reported in [4], which controlled the EFR's slip to ensure the system operates at the maximum power point. However, due to issues related to machine saturation, it is recommended to avoid operating at frequencies below the nominal, i.e.,  $\omega_i \leq 376.99$  rad/s, with  $3PP_g \leq R \leq 6PP_{efr}$ . This precaution ensures that the system consistently operates at the Maximum Power Point Tracking.

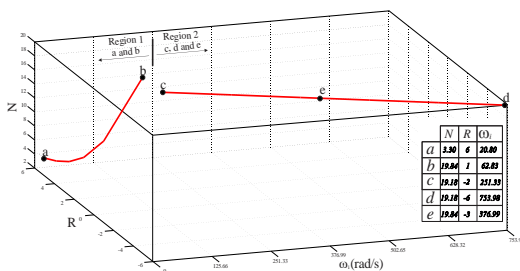


Fig. 9. Influence of  $R$  and  $N$  on the angular velocity of the EFR.

## 7. Conclusion

The conclusions derived from this study are instrumental in directing the future development of the Electromagnetic Frequency Regulator (EFR). Three potential strategies are proposed:

1. Achieving the MPPT with a constant number of poles in both the EFR and the generator, while employing an adjustable transformation ratio in the speed multiplier, as suggested in [9].

2. Utilizing a fixed number of poles in both the generator and EFR, along with a constant transformation ratio in the speed multiplier, and pursuing MPPT through the control of EFR slip, as discussed in [4].
3. The contribution of this study is the exploration of MPPT through the adjustment of the EFR drive frequency ( $\omega_i$ ), with a variable number of poles and a fixed transformation ratio in the speed multiplier. Specifically, in this scenario, it is recommended to ensure that the number of poles in the EFR ( $P_{efr}$ ) is greater than the number of poles in the generator ( $P_g$ ), a prerequisite for  $\omega_i \geq \omega_s$ . This approach enhances inverter performance and mitigates the risk of EFR saturation.

## Acknowledgement

The authors would like to thank the Coordination of Superior Level Staff Improvement (CAPES) – Brazil for the financial support.

## References

- [1] Su, W., Wang, J., Roh, J., "Stochastic energy scheduling in microgrids with intermittent renewable energy resources," in *IEEE Transactions on Smart Grid*, vol. 5, no. 4, pp. 1876-1883, July 2014, doi: 10.1109/TSG.2013.2280645.
- [2] K. Dietrich, J. M. Latorre, L. Olmos and A. Ramos, "Demand Response in an Isolated System With High Wind Integration," in *IEEE Transactions on Power Systems*, vol. 27, no. 1, pp. 20-29, Feb. 2012.
- [3] A. O. Bissiriou, R. L. d. A. Ribeiro and T. d. O. A. Rocha, "Contributions to energy management of single-phase AC microgrids used in isolated communities," in *27th International Conference on Electricity Distribution (CIRED 2023)*, Rome, Italy, 2023, pp. 3811-3815, doi: 10.1049/icp.2023.0716.
- [4] Ramos, T., Medeiros Júnior, M. F., Pinheiro, R., & Medeiros, A. (2019). "Slip control of a squirrel cage induction generator driven by an electromagnetic frequency regulator to achieve the maximum power point tracking". *Energies*, 12(11), 2100.
- [5] Blasques, L. C. M., & Pinho, J. T. (2012). Metering systems and demand-side management models applied to hybrid renewable energy systems in micro-grid configuration. *Energy Policy*, 45, 721-729.
- [6] Pinho, J. T., Barbosa, C. F. O., Pereira, E. J. S., Souza, H. M. S., Blasques, L. C. M., Galhardo, M. A. B., & Macêdo, W. N. (2008). "Sistemas híbridos". *Brasília: Ministério de Minas e Energia*.
- [7] Gupta, A., Doolla, S., & Chatterjee, K. (2017). "Hybrid AC-DC microgrid: Systematic evaluation of control strategies". *IEEE Transactions on Smart Grid*, 9(4), 3830-3843.
- [8] P. V. Silva, R.F. Pinheiro, A. O. Salazar, L. P. Santos Jr, & J. D. Fernandes, "Um Novo Sistema para Controle de Velocidade em Aero geradores Utilizando o Regulador Eletromagnético de Frequência," in *Eletrônica de Potência*, p. 254-262, 2015.
- [9] Patriota, A. S. L. (2020). "Utilização de energia eólica com transmissão hidrostática acoplada ao regulador eletromagnético de frequência" — *Master's thesis, Universidade Federal do Rio Grande do Norte*.
- [10] Silva, P. V., et al. "Performance analysis of a new system for speed control in wind turbines." *Renew. Energy Power Qual. J* 1 (2015): 455-460.
- [11] T. F. do Nascimento, E. A. F. Nunes and A. O. Salazar, "Modeling and Controllers Design for an Electromagnetic Frequency Regulator Applied to Wind Systems," *2021 Brazilian Power Electronics Conference (COBEP)*, João Pessoa, Brazil, 2021, pp. 1-8, doi: 10.1109/COBEP53665.2021.9684101.
- [12] Crisóstomo, D. C., do Nascimento, T. F., Nunes, E. A., Villarreal, E., Pinheiro, R., & Salazar, A. (2022). "Fuzzy control strategy applied to an electromagnetic frequency regulator in wind generation systems". *Energies*, 15(19), 7011.
- [13] Fitzgerald, Arthur Eugene, Charles Kingsley, and Stephen D. Umans. "Electric machinery." (2003).